Science of the Total Environment 899 (2023) 165683

Contents lists available at ScienceDirect

Science of the Total Environment

journal homepage: www.elsevier.com/locate/scitotenv

Microplastic transport dynamics in surcharging and overflowing manholes

Ben Stride [a,*], Charlotte Dykes [a], Soroush Abolfathi [a], Modupe Jimoh [a], Gary D. Bending [b], Jonathan Pearson [a]

[a] School of Engineering, University of Warwick, Coventry CV4 7AL, UK
[b] School of Life Sciences, University of Warwick, Coventry CV4 7AL, UK

ARTICLE INFO

Editor: Dimitra A Lambropoulou

Keywords:
Mixing
Polyethylene
Deconvolution
Dead zone
Pollution transport
RTD

ABSTRACT

The transport of microplastics within urban water systems remains poorly understood, with little prior research on their behaviour within manhole configurations. This study represents the first to measure and model the transport dynamics of microplastics within circular and square manholes under different hydraulic scenarios. The transport and fate of polyethylene (PE) was quantified and compared to solutes (Rhodamine WT dye) using energy losses, residence time distributions (RTDs), and mixing models within surcharging and overflowing manholes. The bulk mass of solute and PE concentrations followed similar flow paths across all conditions except for 17.3 ± 7.9 % of PE mass that was immobilized in a dead zone above the inlet pipe for manholes with a surcharge to pipe diameter ratio ≥2. Consequently, these microplastics only exit after a significant change in hydraulic regime occurs, causing microplastics to be at risk of being contaminated over a prolonged duration. No significant mixing differences for PE and solutes were found between manhole geometries. The deconvolution method outperformed the ADZ model with goodness of fit (R_t^2) values of 0.99 (0.60) and 1.00 (0.89) for PE and solute mixing, respectively. This establishes the deconvolution method as the most accurate and appropriate model to accurately predict microplastic mixing in manholes and urban drainage systems.

1. Introduction and background

Limited data is available on how pollutants move from sewer systems to surface flood water (Beg et al., 2020) and a recent review by Österlund et al. (2023) confirms that research on microplastics, plastics >1 μm and <5 mm (Frias and Nash, 2019), in urban areas is "data-poor". Despite the ubiquity of microplastics, little prior research has taken place on microplastic movement in manholes. Previous research has focused on soluble pollution transport in circular manholes, ignoring the effects of solid particles or square manholes (Beg et al., 2017; Guymer et al., 2005; Jimoh and Abolfathi, 2022). Microplastics can act as a pathway for disease-carrying pathogens that adhere to their surfaces, enabling them to survive for extended periods (Zhang et al., 2022) and many questions remain on their toxicity and potential long-term effects (Jenner et al., 2022; Sana et al., 2020). During flooding events, manholes in combined sewer systems become surcharged, creating complex pollutant mixing conditions that pose a dangerous risk of pathogenic and chemical contamination (Beg et al., 2020; de Man et al., 2014; Schreiber et al., 2019; Sonnenwald et al., 2021). Quantifying the resultant microplastic concentrations in surcharging and overflowing manholes based off previously proven solute transport theory is therefore critical for the optimum design and operations of wastewater infrastructures.

Previous results have indicated that microplastics of a near neutral buoyancy behave in the same manner as a solute in waves (Abolfathi et al., 2020), uniform open channels (Cook et al., 2020), and vegetated streams (Stride et al., 2023) under the assumption that they are well-mixed over depth. Globally, polyethylene (PE) with a near-neutral buoyancy of between 0.91 and 0.97 g/cm^3 is the most produced plastic polymer due to its use in plastic bags, household items, and packaging, encompassing approximately 40.5 % of the world's plastic polymer demand (Ziccardi et al., 2016; Jones et al., 2020; Plastics Europe, 2021). However, given how surcharging manholes emulate dead zones within rivers (Sokáč and Velísková, 2021), the slight difference between the density of PE and water may cause dispersion differences with movement due to advection being interrupted.

Mixing dynamics between sewer pipes and manholes are dominated by advection and dispersion due to strong local velocities, resulting in the concentration of a solute varying temporally and spatially (Beg et al., 2020; GebreEgziabher and Demissie, 2020; Sokáč and Velísková, 2021).

* Corresponding author.
E-mail addresses: ben.stride@warwick.ac.uk (B. Stride), Soroush.Abolfathi@Warwick.ac.uk (S. Abolfathi).

https://doi.org/10.1016/j.scitotenv.2023.165683
Received 18 May 2023; Received in revised form 17 July 2023; Accepted 18 July 2023
Available online 20 July 2023

Surcharge depth ratios ($\frac{S}{P_d}$) have previously been utilized to predict complete mixing in 180° piped manholes with no plunging present, where S is the surcharge height (m), and P_d is the pipe diameter. Guymer et al. (2005) and Lau et al. (2008) found that above a surcharge ratio of between 2 and 2.5, the bulk mass of solutes advect straight through the system leaving little retention time for mixing. Flows containing surcharges below this ratio are completely mixed in a vortex whilst surcharges above present two distinct flow regimes in the same flow (Guymer et al., 2005). More recent studies have utilized submerged jet theory where the jet flow starts expanding as it proceeds towards the outlet pipe due to the through-flowing water from the inlet pipe accelerating the entrained water in the manhole causing surplus discharge to be lost (Beg et al., 2017; Kerenyi et al., 2007; Mark and Ilesanmi-Jimoh, 2016; Stovin et al., 2008; Stovin et al., 2010). Beg et al. (2017) proposed that as the jet flow reaches the entrance of the outlet pipe in circular manholes it expands and a portion hits the manhole wall at the top of the outlet, proceeding vertically upward into a dead zone at the top of the manhole (Sokáč and Velísková, 2021). At these higher surcharge depths, if a significant pollutant concentration experienced this phenomenon, it would drastically increase manhole retention times with some being immobilized until the manhole overflows and a flooding scenario takes place.

Several methods can be used to describe flow properties in manholes. Among the most common are Reynolds numbers (R_e) and head losses (ΔH). Head losses in pipes have historically been well analyzed through hydraulic roughness and Pedersen and Mark's (1990) equation, with head loss coefficients (K) proven to be dependent on available surcharges (Beg et al., 2019). Manhole head losses are not well described for all manhole configurations, and there has been little quantification of head losses in overflowing manholes caused by full and partial blockages. The current understanding of head losses in manholes can be described by Beg et al. (2017) and Guymer et al. (2005), finding that regardless of benching setups or manhole diameter, manholes had a higher K at lower surcharge depths within circular manholes. Therefore, it is reasonable to assume that a higher K is present within lower surcharge depths where more mixing occurs. Commonly used equations typically yield head losses that are an order of magnitude larger than the values encountered in laboratory experiments (Pedersen and Mark, 1990).

RTDs (residence time distributions) and CRTDs (cumulative RTDs) are currently widely accepted as the most appropriate method of modelling and evaluating pollutant concentrations in manholes (Guymer and Stovin, 2011; Jimoh and Abolfathi, 2022; Sonnenwald et al., 2015; Sonnenwald et al., 2021). RTDs show the outlet response to an instantaneous concentration injection at the systems inlet, thus evaluating the hydraulic performance of the system (Guymer and Stovin, 2011). Specifically, RTDs describe the residence time and provide a measure of the mixing response of a concentration within the surrounding system or environment (Danckwerts, 1953; Sonnenwald et al., 2015). CRTD's present an alternative way to present concentration response data and are the integral form of the RTD over time. Typical shapes of RTDs (C-diagrams) and CRTDs (F-diagrams) for representative types of a manhole system are shown in Sonnenwald et al. (2021). A variety of parameters and indices can be derived from RTDs and CRTDs to describe the hydraulic performance of a system. A widely accepted approach is to utilize the time elapsed between the initial injection at the inlet and a percentage of the concentration mass reaching the outlet, denoted as t_i (Stovin et al., 2008).

This study represented the first to measure and model the transport dynamics of microplastics within circular and square manholes under different hydraulic scenarios. Cook et al.'s (2020) microplastic staining technique using Nile red dye was adopted to trace PE's behaviour within surcharged manholes of different shapes, depths, and discharges. The aim was to improve the current understanding of the underlying physical mechanisms that govern microplastic mixing and hydraulic energy losses within sewer systems and inform future wastewater infrastructure projects. The transport characteristics of microplastics and soluble pollutants between the sewer pipe and manhole were determined by RTDs. Energy losses were analyzed using manometers to calculate K. RTDs and CRTDs for spherical neutrally buoyant PE were calculated and compared with those measured from the representative solute Rhodamine WT dye. Current mixing models were utilized to see where they are applicable for predicting neutrally buoyant microplastic dispersion. The data can then be used to validate and expand current methods predicting microplastic and soluble pollution concentrations downstream of a manhole.

2. Methods

2.1. Manhole setup and processes

Head loss and concentration data was gathered in a recirculating system with 6.1 m long pipes of a 0.05 m internal diameter made of glass reinforced plastic. The pipe was connected to the manhole at a 180° angle either side for straight flow from inlet to outlet. The outlet pipe emptied into a 2.0 × 2.0 × 1.0 m dimensioned storage tank that recirculated the flow back into the inlet pipe (Fig. 1). For practical applications, the experimental set up consisted of clean and smooth pipe manhole conditions, eliminating the effects of friction from the sewer walls, scaling, or bottom sediment that would be expected to be seem in a real-world sewer system. The circular and square manholes had diameters of 0.4 m with a minimum manhole depth of 0.055 m to enable full flow conditions in the outlet pipe. The main pipe flow length was 6.5 m long including the manhole diameter. The top of the pipe was 0.05 m above the manhole bottom for surcharge calculations within both manholes.

Inlet pipe discharges (Q) were set using a SIEMENS F M MAG6000 electromagnetic flow meter located between the pump and the flow inlet and adjusted through a remote control. Fluorometers designed to detect Rhodamine WT's excitation/emission wavelengths of 555/580 nm were used to quantify the transport of stained microplastics (Cook et al., 2020; Abolfathi et al., 2020; Stride et al., 2023). For dye, 0.6 ml of Rhodamine WT was extracted from a stock concentration of 10^7 to create a solution of 6000 ppb in 1 L for surcharge tests and 10,000 ppb for the overflow tests using a micropipette. 20 ml of the resulting solution was well mixed within a syringe for each injection. For microplastics, 0.5 g of Nile Red (technical grade, N3013, Sigma-Aldrich) stained polyethylene (434272, Sigma-Aldrich) was well-mixed into 10 ml of water at room temperature within a syringe for each injection. Each injection was situated in the same position after the pump and before the flow inlet pipe began (1.55 m before the first fluorometer), to ensure the injections were well mixed before entering the main pipe length (Fig. 1). The distance between the center of the second fluorometer (F2a) and (F3a) third fluorometer was 1.4 m for the variable and surcharge tests, 2.7 m between the first (F1) and second fluorometer (F2b) for the overflow tests, and 4.4 m between F1 and the fourth fluorometer (F4) for the PB overflow outlet tests. F3b was used as a data check for the overflow scenarios.

A summary of all the flow conditions and parameters is provided in Table 1. Six experimental conditions were employed containing initial inlet pipe discharges of 0.00062. 0.00102, and 0.00142 m^3/s, each with five replicates (n) and corresponding inlet pipe R_e of 15,737, 25,887, and 36,037. The six conditions included a variable depth, three surcharge depths of 0.1, 0.25, 0.4 m, and a partially (PB) and fully blocked (FB) flooding scenario (Table 1). PB data was gathered from both the outlet pipe and top of the manhole resulting in an extra condition for the same injections in Table 1. Surcharge depths were created through opening and closing the sluice gate located in the outlet pipe (SG1), along with a variable depth that changed naturally with discharge. A sluice gate height of 0.01 m was used for the variable depths to prevent air bubbles from interfering with the instruments located along the outlet pipe. SG2 was used to maintain a constant depth for consistency and readings in the overflow structure from F3b (Fig. 1). Sluice gate adjustments were

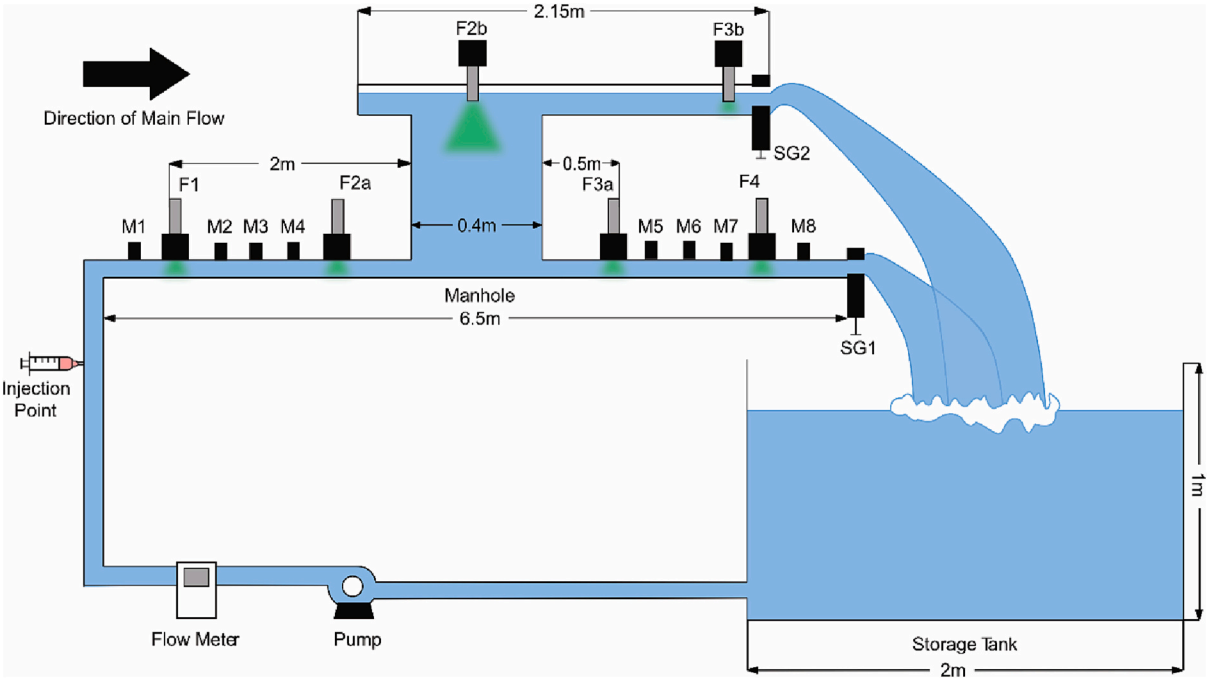

Fig. 1. 2D visualization of manhole experimental setup (not to scale).

noted before each change in discharge or depth. Surcharge depths were calculated by subtracting the distance from the top of the inlet and outlet pipes from the water depth.

For surcharge tests, one Turner Designs Cyclops-7 fluorometer was positioned either side of the manhole (F2a & F3a), calibrated, and set to a x10 gain. F2a and F3a used in the surcharge tests were moved to the overflow structure (labelled F2b and F3b) and set to a x100 gain for the PB and FB scenarios (Table 1) due to the lower concentrations. F1 and F4 were subsequently used to determine inlet and outlet pipe concentrations in the PB and FB scenarios. Data was gathered at time intervals every 0.05 s (20 Hz) for the variable and surcharge tests and 0.1 s (10 Hz) for the overflow tests through an automatic recorder, logging voltage changes in the water column. 20 s was allowed between the concentration data first being logged and the dye or PE being vertically injected. Similarly, logging stopped at least 20 s after fluorescence was no longer detected. Logging ran for approximately 5 min during the variable and surcharge tests and 25 min and 15 min for the partially and fully blocked scenarios.

Three head loss measurements were taken at each of the eight manometers (M1-M8) for each flow condition within both the circular and square manholes then averaged. Any air bubbles were removed prior to recording. The resting water pressure for each manometer was noted before the pump was turned on to calculate the change in height. The eight manometers were implemented at 0.5 m intervals with four in the inlet pipe and four in the outlet pipe, each connected to individual stilling tubes (Fig. 1). For each discharge and surcharge, the height of the water in each of the eight stilling tubes was measured and recorded to the nearest millimetre to determine the head loss at each discharge. ΔH was determined by subtracting the average linear upstream head loss from the average linear downstream head loss measurements to predict ΔH at the centre of the manhole for each configuration and discharge. Subsequently, due to our setup containing no benching, plunging, or different pipe angles, K was theoretically predicted using Pedersen and Mark's (1990) equation:

$$K = \frac{\Delta H}{\left(\frac{u_o^2}{2g}\right)}, \tag{1}$$

where u_o is the mean velocity (m/s) in the outlet pipe and g is acceleration due to gravity (m^2/s).

2.2. RTD indices

t_n represents the normalised retention time, which is the theoretical time for a system to discharge its entire volume and occurs when $\frac{tQ}{V} = 1$, where V is the volume of water in the manhole. If a steep rise occurs before t_n a restricted channel or idealised flow path is present and short-circuiting takes place due to the system being dynamic and not uniform (Sonnenwald et al., 2021). t_n was theoretically calculated by dividing V by Q in Eq. (2):

$$t_n = \frac{V}{Q}. \tag{2}$$

Time was subsequently normalised through t_n to illustrate mixing independent of manhole diameter, discharge, or surcharge depth and increase comparability (Sonnenwald et al., 2021). Many different short-circuiting indices can be obtained from RTDs other than t_n, with the most common being t_m and t_p which represent the mean and peak concentration times, respectively. Other short-circuiting indices utilize the time taken for a percentage to arrive at the outlet such as t_1,t_{10},t_{16}, t_{50}, and t_{70} (Persson, 2000; Sonnenwald et al., 2021; Stovin et al., 2008). For a comprehensive analysis, a range of indices including, t_n, t_m, t_{16}, and t_{50} were selected for this study.

Another way to quantify short-circuiting is by dividing the above indices by each other. Large values correspond to low or zero short-circuiting and small values indicate large amounts of short-circuiting. There are several methods of calculating the short-circuiting parameter (S_C) (e.g., Ta and Brignal, 1998; Persson, 2000; Stovin et al., 2008; Goodarzi et al., 2022). With Ta and Brignal (1998), Persson (2000), and Goodarzi et al. (2022) focusing on Wetland short-circuiting, Stovin et al.'s (2008) proposed formula was chosen as the most appropriate parameter for manhole short-circuiting in Eq. (3):

$$S_C = \frac{t_{50}}{t_n}. \tag{3}$$

Hydraulic efficiency (*HE*) presents another index capable of

quantifying manhole flow properties by encompassing the effects of short-circuiting, recirculation, and dead zones (Persson, 2000), and was calculated through Eq. (4):

$$HE = \frac{t_p}{t_n}. \tag{4}$$

High *HE* values mean the pollutant in question is retained within the system for a sufficient time compared to low values indicating the pollutant is advecting straight through.

2.3. Modelling manhole mixing

The conventional approach of modelling mixing in pipe flow is using the ADE model by adapting Taylor's (1954) equation. However, the ADE model does not consider the effects of dead zones that can dominate dispersion processes in certain environments. Dead zones represent areas where advective flow is interrupted and stored momentarily in an area of mixing. Therefore, dead zones can create distinct retention times where mixing occurs, enabling a substance to disperse before re-joining the main flow. Manholes emulate these dead zones where there is a time delay between a solute leaving the inlet pipe and entering the outlet pipe depending on the flow rate and water depth present within the manhole itself when compared to straight pipe flow (Guymer and O'Brien, 2000; Sokáč and Velísková, 2021). Beer and Young (1983) and subsequently Wallis and Beven (1989) established an ADZ model based on Taylor's (1954) original formulae but also considered dead zone effects on dispersion by utilizing a discrete-time equation for predicting the temporal distributions of concentration data downstream:

$$c(x_2,t) = -\alpha c(x_2,t-1) + (1+\alpha)c(x_1,t-t_s), \tag{5}$$

where $c(x_2,t)$ is the concentration in the outlet pipe and $c(x_1,t)$ in the inlet pipe, the ADZ variable $\alpha = -exp\left(\frac{-\Delta t}{T}\right)$, Δt is the sampling interval (s), $T = \bar{t} - t_d$ and is the dead zone residence time. $\bar{t}$ is the travel time to the centroid (μ) in seconds, t_d is the time delay before the first arrival of the concentration distribution (s), and t_s is the advective time delay in sampling intervals to the nearest lower integer ($\frac{t_d}{\Delta t}$).

An R_t^2 parameter can then be used to measure the goodness of fit of a predicted downstream temporal concentration profile $p(x_2,t)$ in relation to the measured downstream data $c(x_2,t)$ and was calculated through Eq. (6):

$$R_t^2 = 1 - \left[\frac{\sum_{t=1}^{n}\left[c(x_2,t) - p(x_2,t)\right]^2}{\sum_{t=1}^{n} c(x_2,t)^2}\right]. \tag{6}$$

An R_t^2 value of 1.0 indicates a perfect fit from the model in question and values <1.0 indicate a weaker predictive capability (Guymer and Stovin, 2011). The ADZ produces a concentration distribution purely from the upstream concentration profile in the inlet pipe and is not very dependent on flow characteristics. Meaning for certain conditions it doesn't predict the Gaussian shaped portion of the response curves well due to the complexity of the flow, which may lead to peak concentrations being over or under predicted and potentially misleading goodness of fit values (Guymer et al., 2005; Guymer and Stovin, 2011).

Recent research indicates deconvolving RTDs provides a more flexible approach to modelling solute transport than fitting parametrised models such as the advection-dispersion equation model (ADE) or aggregated dead-zone model (ADZ) (Guymer and Stovin, 2011; Rutherford, 1994; Sonnenwald et al., 2014; Sonnenwald et al., 2015). After a thorough review Sonnenwald et al. (2014) proposed a deconvolution algorithm based on system theory to determine RTDs based on raw data within urban drainage systems which was adopted by Jimoh and Abolfathi (2022) for overflowing manholes. Deconvolution utilizes RTDs to predict mixing independent of the upstream concentration distribution and instead considers the relationship between the upstream and downstream concentrations of a system through a convolution integral (Jimoh and Abolfathi, 2022; Sonnenwald et al., 2021):

$$c(x_2) = \int_0^t c(x_1, t-\tau)E(\tau)d\tau, \tag{7}$$

where $E(\tau)$ denotes the RTD and τ is the integration variable. A Lagrangian function (L) was then maximized, to combine an entropy function measuring the shape of the RTD ($S(\widehat{E})$) and a constraint function measuring the goodness-of-fit between the predicted and measured downstream profiles (C), to solve the RTD (Sonnenwald et al., 2015):

$$L(\widehat{E},\lambda) = C + \lambda S(\widehat{E}), \tag{8}$$

where $\widehat{E}$ represents each individual data point of the RTD and λ is Lagrange multiplier defined during maximization. C and $S(\widehat{E})$ can be determined through different methods outlined in Sonnenwald et al. (2014).

2.4. Concentration data analysis

Background concentrations were removed by subtracting the mean concentration of the first 15 s before the tracer injection. The resulting tracer data was captured in volts and converted to concentrations (ppb for dye, g/l for PE) using linear calibration curves for both dye and PE with $r^2 \geq 0.98.5$ for each fluorometer (Fig. S1a & b). A running average containing 1% of the total data points for each replicate was used for smoothing the variable and surcharge conditions. A different running average with a window of 1.8 s was used for overflow tests for the inlet and outlet pipe concentrations (F1 & F4) to approximate the same running average used for the variable and surcharge conditions due to the longer logging lengths. 1% of the total data points was once again used for concentrations at the top of the overflowing manhole (F2b).

Cut-off values for each distribution curve were defined where the concentration in the tail reached 1% of the peak concentration for the variable and surcharging tests, and the second negative value for the overflow tests due to low peak concentrations as a result of larger retention times. Velocities were determined through Eqs. (9) & (10), depending on the experimental condition:

$$u = \frac{x_{3a} - x_{2a}}{\mu_{3a} - \mu_{2a}}, \tag{9}$$

where x is distance (m) and μ is the time to centroid (s). To capture mean velocities in the overflow scenarios, velocities were calculated using fluorometers F1 and F2b instead of F2a and F3a (Fig. 1) resulting in:

$$u = \frac{x_{2b} - x_1}{\mu_{2b} - \mu_1}. \tag{10.1}$$

For the overflow PB outlet scenario velocities were calculated from the same pulse injection but F2b positioned at the top of manhole was replaced with F4 in the outlet pipe (Fig. 1):

$$u = \frac{x_4 - x_1}{\mu_4 - \mu_1}. \tag{10.2}$$

Mass recovery (MR) percentages were determined between the inlet pipe and exit via the outlet pipe or top of the manhole, depending on the condition being tested. This was achieved by dividing the first moment of area (M_0) in the exit by M_0 in the inlet pipe and multiplying the answer by 100, with the aim of calculating how much of the injected dye and PE mass concentrations had left the system. Cut-offs, smoothing, and R_t^2 for the deconvolution model (DM) were selected using the same processes outlined above and positions of the RTD sample points were created using slope based fast-Fourier transformation deconvolution and Blackman-Tukey windowing (Sonnenwald et al., 2014). 40 sample points and 350 iterations, as recommended by Sonnenwald et al. (2014), were selected for deconvolution with an R_t^2 based constraint (C) and a

Table 1
Summary of experimental flow parameters and results for both circle and square manholes. Mean velocities were calculated from Eqs. (10) & (11). Indices below line are calculated from the top of the manhole and not the outlet pipe.

n	Exp. condition	Inlet Q (m^3/s)	Inlet pipe reynolds number (*Re*)	Flow depth (m)	Surcharge depth ratio ($\frac{S}{P_d}$)	Circle observed head loss (ΔH)	Square observed head loss (ΔH)	Circle mean velocity (m/s)	Square mean velocity (m/s)	Mean goodness of fit (R_t^2)			
										ADZ Dye	ADZ PE	DM Dye	DM PE
5	Variable	0.00062	15,737	0.054	0.08	0.0015	0.0021	0.1407	0.1149	0.99	0.95	1.00	1.00
5	Variable	0.00102	25,887	0.085	0.70	0.0158	0.0149	0.1359	0.1071	1.00	0.88	1.00	1.00
5	Variable	0.00142	36,037	0.122	1.44	0.0311	0.0291	0.1322	0.1119	1.00	0.94	1.00	1.00
5	0.1 m Surcharge	0.00062	15,737	0.150	2.00	0.0026	0.0046	0.0641	0.0815	0.97	0.87	1.00	1.00
5	0.1 m Surcharge	0.00102	25,887	0.150	2.00	0.0075	0.0086	0.1032	0.1100	0.98	0.79	1.00	0.99
5	0.1 m Surcharge	0.00142	36,037	0.150	2.00	0.0334	0.0229	0.1864	0.1160	0.98	0.89	1.00	1.00
5	0.25 m Surcharge	0.00062	15,737	0.300	5.00	0.0035	0.0031	0.2433	0.3068	0.69	0.00	1.00	0.99
5	0.25 m Surcharge	0.00102	25,887	0.300	5.00	0.0080	0.0080	0.4700	0.4954	0.68	0.05	1.00	0.97
5	0.25 m Surcharge	0.00142	36,037	0.300	5.00	0.0151	0.0125	0.5705	0.6058	0.69	0.20	1.00	1.00
5	0.4 m Surcharge	0.00062	15,737	0.450	8.00	0.0009	0.0004	0.2940	0.3100	0.66	0.07	1.00	0.99
5	0.4 m Surcharge	0.00102	25,887	0.450	8.00	0.0072	0.0056	0.4954	0.5281	0.70	0.00	1.00	0.99
5	0.4 m Surcharge	0.00142	36,037	0.450	8.00	0.0137	0.0128	0.6957	0.7194	0.68	0.13	1.00	1.00
5	Overflow PB Outlet	0.00062	15,737	0.700	13.00	−0.0002	−0.0033	0.2530	0.2568	0.91	0.38	0.99	0.99
5	Overflow PB Outlet	0.00102	25,887	0.700	13.00	−0.0061	−0.0097	0.2933	0.3189	0.98	0.55	1.00	0.99
5	Overflow PB Outlet	0.00142	36,037	0.700	13.00	−0.0156	−0.0209	0.3246	0.3538	0.97	0.82	1.00	1.00
5	Overflow PB	0.00062	15,737	0.700	13.00	−0.0002	−0.0033	0.0106	0.0082	0.96	0.89	1.00	1.00
5	Overflow PB	0.00102	25,887	0.700	13.00	−0.0061	−0.0097	0.0218	0.0168	0.96	0.87	0.99	1.00
5	Overflow PB	0.00142	36,037	0.700	13.00	−0.0156	−0.0209	0.0337	0.0266	0.97	0.89	1.00	1.00
5	Overflow FB	0.00062	15,737	0.700	13.00	−0.0037	−0.0038	0.0191	0.0150	0.98	0.87	1.00	1.00
5	Overflow FB	0.00102	25,887	0.700	13.00	−0.0101	−0.0097	0.0283	0.0233	0.99	0.73	1.00	1.00
5	Overflow FB	0.00142	36,037	0.700	13.00	−0.0180	−0.0206	0.0376	0.0334	0.97	0.79	1.00	1.00

Table 2
R_e of surcharge and overflow conditions tested.

	Circle manhole							Square manhole						
Inlet Q (m^3/s)	Variable	0.1	0.25	0.4	PB Outlet	PB	FB	Variable	0.1	0.25	0.4	PB Outlet	PB	FB
0.00062	7017	3196	12,137	14,667	12,621	529	953	5731	4066	15,303	15,466	12,811	409	748
0.00102	6777	5149	23,447	24,713	14,631	1087	1412	5342	5487	24,715	26,346	15,908	838	1162
0.00142	6592	9298	28,462	34,706	16,193	1681	1876	5583	5787	30,218	35,890	17,649	1327	1666

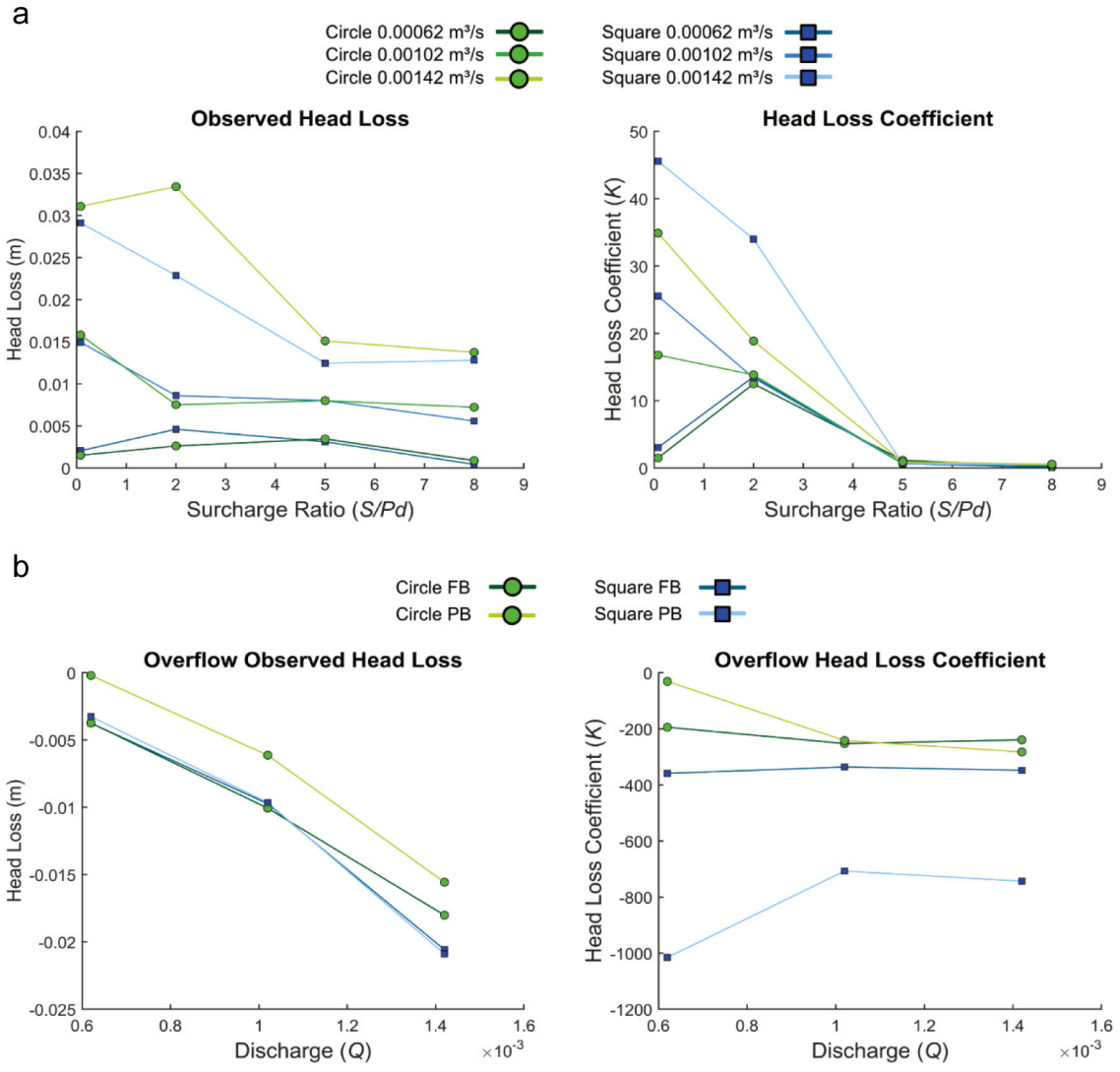

Fig. 2. a. Observed head loss and *K* of circle and square manholes plotted against the surcharge ratio.
b. Observed head loss and *K* of circle and square manholes plotted against discharge for the overflow conditions.

maximum entropy minimizer ($S(\widehat{E})$). A linear moving average was used to interpolate the remaining points.

3. Results

3.1. Reynolds numbers and head losses

Transitional flow does not occur for any condition as shown in Table 2. All variable and surcharge conditions in both manhole types were turbulent. The type of flow in the overflow conditions was considered laminar, with more pronounced laminar flow observed with decreasing *Q*. More turbulent flow at the same *Q* was seen in the variable surcharge condition in the circle manhole compared to the square configuration. The opposite was seen for the other surcharge conditions except for the 0.1 m fixed surcharge at 0.00142 m^3/s, with a R_e of 9298 compared to 5787 in the square manhole. For all fixed surcharge conditions, turbulence increased with flow rate, unlike the variable surcharge where R_e were highest at the slowest *Q*. Head losses of the square and circle manholes remained similar at discharges of 0.00062 and 0.00102 m^3/s, but for 0.00142 m^3/s at an $\frac{S}{P_d}$ of 2 the circular manhole experienced greater head loss (Fig. 2a). Both manholes experienced greater head losses at higher discharges with no significant differences found between manhole geometries (Welch's *t*-test $p > 0.05$). *K* was higher and displayed greater variability for $\frac{S}{P_d} \leq 2$ where at 0.00062 m^3/s *K* increased with $\frac{S}{P_d}$. There was a major loss in *K* between a $\frac{S}{P_d}$ of 2 and 5 for both the circle and square manholes ranging from 11.36 to 33.23

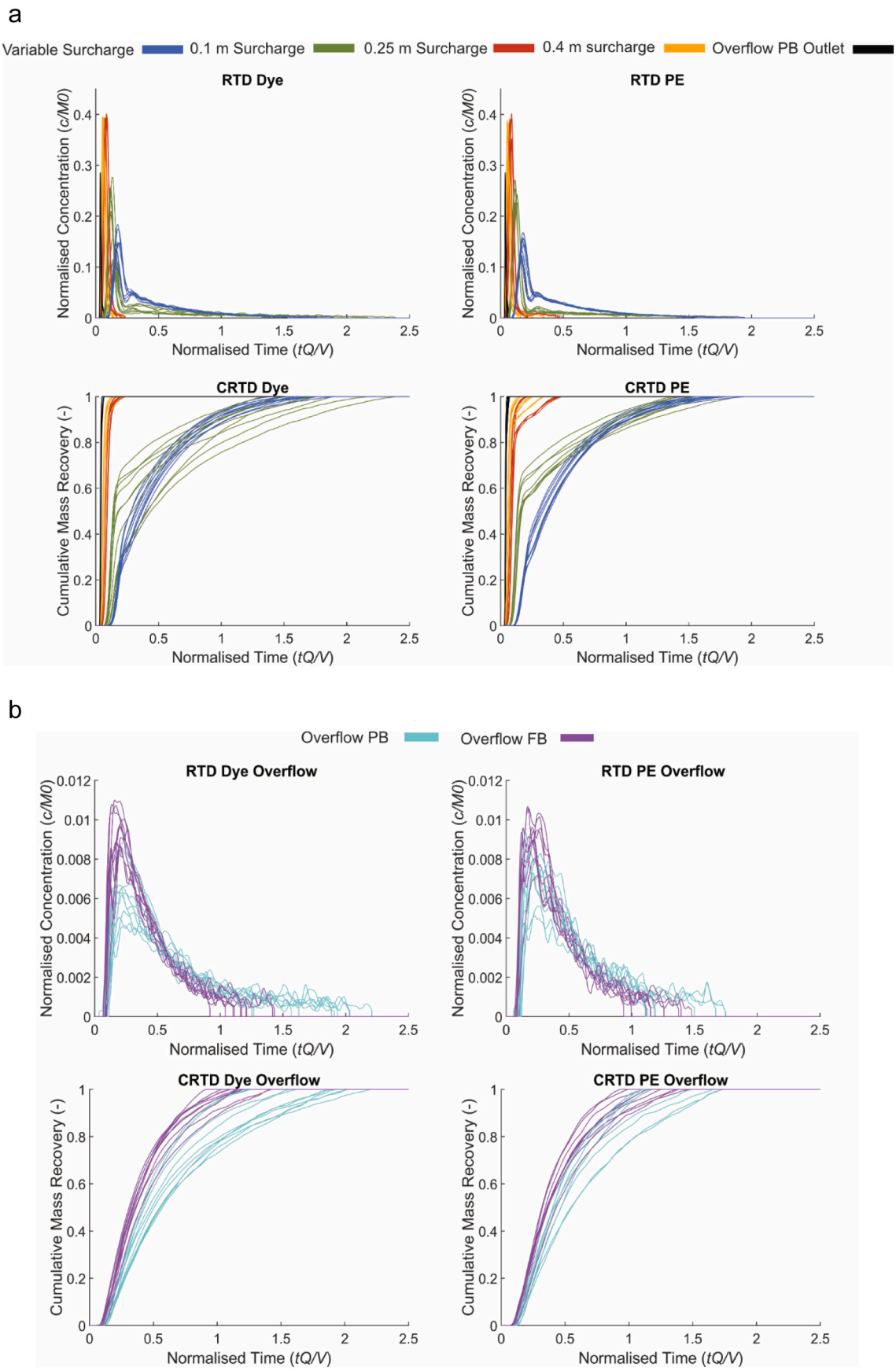

Fig. 3. a. RTD and CRTD profiles from the outlet pipe for both dye and PE at 0.00102 m^3/s: (a) Dye RTDs, (b) PE RTDs, (c) Dye CRTDs, (d) PE CRTDs. b. Overflow RTD and CRTD profiles from the top of the manhole for both dye and PE at 0.00102 m^3/s.

Table 3
Mean RTD indices for both dye and PE for all discharges and conditions across circle and square manholes. Indices below the line are calculated from the top of the manhole and not the outlet pipe, MRs labelled with an asterisk (*) are inflated due to the larger time intervals in the inlet pipe.

		Circle								Square							
		Dye				PE				Dye				PE			
Condition	Inlet Q (m^3/s)	t_n (s)	t_m (s)	S_c	HE	MR (%)	t_m (s)	S_c	HE	MR (%)	t_n (s)	t_m (s)	S_c	HE	MR (%)	t_m (s)	S_c	HE	MR (%)
Variable	0.00062	42.62	13.69	0.20	0.17	93.73	14.10	0.20	0.17	84.46	45.61	15.53	0.20	0.16	91.16	16.16	0.20	0.16	80.31
Variable	0.00102	29.73	12.80	0.31	0.18	96.50	13.25	0.32	0.18	75.43	32.59	15.72	0.37	0.17	94.85	15.80	0.38	0.17	74.76
Variable	0.00142	24.63	12.81	0.41	0.18	100.09	12.66	0.40	0.18	90.53	27.58	14.50	0.41	0.15	95.83	14.85	0.41	0.15	77.14
0.1 m Surcharge	0.00062	62.08	28.15	0.30	0.12	94.40	24.74	0.23	0.12	76.88	70.38	21.13	0.14	0.11	82.56	21.44	0.14	0.10	71.40
0.1 m Surcharge	0.00102	37.73	19.01	0.34	0.14	92.54	15.94	0.21	0.13	67.95	42.78	16.26	0.16	0.12	87.96	15.81	0.17	0.12	70.18
0.1 m Surcharge	0.00142	27.11	9.35	0.16	0.14	93.68	10.02	0.17	0.14	74.03	30.73	13.73	0.23	0.13	85.84	14.86	0.26	0.13	78.30
0.25 m Surcharge	0.00062	92.49	9.80	0.09	0.08	66.93	9.96	0.09	0.08	51.79	109.09	8.74	0.07	0.07	62.64	8.48	0.07	0.07	48.83
0.25 m Surcharge	0.00102	56.22	5.60	0.09	0.09	63.20	6.05	0.09	0.09	52.33	66.31	5.36	0.08	0.08	64.87	6.06	0.08	0.07	47.62
0.25 m Surcharge	0.00142	40.38	4.58	0.10	0.10	65.05	5.00	0.10	0.10	55.43	47.63	4.33	0.08	0.08	66.08	4.90	0.09	0.08	51.17
0.4 m Surcharge	0.00062	122.89	8.21	0.06	0.06	65.61	8.93	0.06	0.06	53.82	147.80	8.47	0.05	0.05	61.38	8.64	0.05	0.05	48.33
0.4 m Surcharge	0.00102	74.70	5.33	0.07	0.07	65.58	5.88	0.07	0.06	50.07	89.84	5.33	0.06	0.05	64.32	5.44	0.06	0.05	50.08
0.4 m Surcharge	0.00142	53.66	4.22	0.07	0.07	65.18	3.89	0.07	0.07	53.53	64.53	4.06	0.06	0.06	63.25	4.17	0.06	0.06	50.07
Overflow PB Outlet	0.00062	648.67	20.22	0.03	0.03	78.29*	19.69	0.03	0.03	57.07*	687.42	19.13	0.03	0.03	73.31*	20.16	0.03	0.03	55.53*
Overflow PB Outlet	0.00102	394.29	16.76	0.04	0.04	96.40*	17.08	0.04	0.04	53.89*	417.84	15.48	0.04	0.04	82.58*	15.77	0.04	0.04	66.57*
Overflow PB Outlet	0.00142	283.22	15.13	0.05	0.05	90.32*	15.17	0.05	0.05	71.93*	300.14	14.03	0.05	0.05	89.06*	14.09	0.05	0.05	77.01*
Overflow PB	0.00062	395.28	284.63	0.58	0.19	73.78*	255.94	0.55	0.18	53.91*	434.03	323.75	0.63	0.21	44.68*	349.45	0.72	0.15	42.45*
Overflow PB	0.00102	240.27	135.10	0.45	0.19	97.27*	121.68	0.42	0.20	67.93*	263.82	176.76	0.54	0.18	90.46*	154.40	0.50	0.24	68.52*
Overflow PB	0.00142	172.59	87.84	0.42	0.21	99.31*	77.82	0.39	0.19	83.98*	189.51	111.84	0.48	0.18	101.06*	98.16	0.44	0.24	87.93*
Overflow FB	0.00062	395.28	143.65	0.31	0.14	112.26	147.48	0.32	0.18	74.87	434.03	195.22	0.37	0.16	95.07	172.36	0.34	0.14	81.14
Overflow FB	0.00102	240.27	94.78	0.33	0.18	103.33	100.84	0.35	0.21	68.85	263.82	115.98	0.36	0.21	102.46	121.70	0.38	0.21	83.11
Overflow FB	0.00142	172.59	71.77	0.34	0.20	88.79	78.29	0.37	0.22	86.28	189.51	85.60	0.37	0.17	102.06	81.54	0.36	0.14	77.96

(Fig. 2a). The square manhole displayed a greater K than the circle manhole for the variable scenario, with the difference increasing with discharge. With surcharges being identical for the overflow conditions head loss was plotted against Q in Fig. 2b. Head loss decreases almost linearly with Q for both overflow conditions, thus demonstrating an energy gain. K displays negative values for all scenarios and up to 1015 for the square manhole when the pipe was PB in contrast to the PB circle manhole that has a maximum of 282 (Fig. 2b). K for the FB conditions remains constant with Q for both manholes.

3.2. Dye and PE distributions

Normalised RTD and CRTD profiles for each replicate across all conditions with the Q of 0.00102 m^3/s are plotted in Fig. 3. The x axis was normalised through $\frac{tQ}{V}$, with the same data normalised by t_m in Fig. S2. The y axis was normalised by dividing the concentration (c) by the area (M_0) for the RTDs and the cumulative maximum value for the CRTDs. Three different curves can be seen for the five different surcharge profiles with the 0.25 m and 0.4 m surcharges showing near identical response curves. PB and FB conditions displayed comparable profiles but with the FB demonstrating slightly higher peak concentrations and a steeper rising CRTD profile. 0.25, 0.4 m surcharges and the PB outlet exhibited profiles resembling plug flow except for the last 3–15 % of the cumulative mass. The variable and overflow tests exhibit shallower rising profiles of a much longer duration, whilst the 0.1 m surcharge displays both an initial steep increase proceeded by a shallower rising profile also of a long duration. In most cases except for the PB scenario S_c increased or remained constant with Q. The PB condition showed the inverse which was expected due to RTD indices being calculated from F2b at the top of the manhole and not F4 in the outlet pipe (Fig. 1). S_c values for 0.25 m and 0.4 m surcharges were below 0.1 for the three inlet pipe discharges. S_c increased with Q up to 0.41 for the variable tests and stayed relatively constant between 0.2 and 0.25 for the 0.1 m surcharge (Table 3). S_c could not be differentiated between manholes or dye and PE concentrations except for the 0.1 m surcharge which may have exhibited opposite trends with Q for the circle and square manholes. HE ranged from 0.05 to 0.24 throughout exhibiting an inefficient system of pollutant retention, which is desired in manholes. HE was lowest at higher surcharges of 0.25 and 0.4 m with a maximum value of 0.1.

Both dye and PE displayed comparable transport behaviour throughout all conditions with no significant differences found between manhole geometries. This was confirmed through analogous RTD indices where t_m, t_{16}, and t_{50} were within 20 % of each other across all conditions except for t_{50} at 0.1 m surcharge and 0.00102 m^3/s (Table S1) which demonstrated a larger variability for dye (Fig. 3a). t_m and t_n were similar for both dye and PE across all conditions but far apart from each other, indicating most of the bulk dye and PE concentrations were following the same preferential flow paths. MR for the dye was marginally greater than PE across the six conditions where a significant difference was found (Welch's t-test $p < 0.05$). The most significant influence on the MR of both dye and PE was the larger surcharge depths that resulted in smaller MR rates for both dye and PE. No significant difference was observed when related to Q. Smaller MR values between 47 and 67 % were observed for the higher surcharges of 0.25 and 0.4 m across both geometries. The largest MR differences were for the overflow conditions between dye and PE with an average of 93 % (dye) and 69 % (PE) in the circle manhole and 87 % (dye) and 71 % (PE) in the square manhole. Tracers took longer to exit the system via the top of the manhole in the overflow tests than the variable and surcharge conditions through the outlet pipe as expected. The extra pipe distance due to the moving of fluorometer F2 for the overflow tests in Fig. 1 only accounted for approximately five, three, and two seconds to t_m for the 0.00062, 0.00102, and 0.00142 m^3/s discharges respectively. Across all RTD indices, most concentrations moving through the square manhole

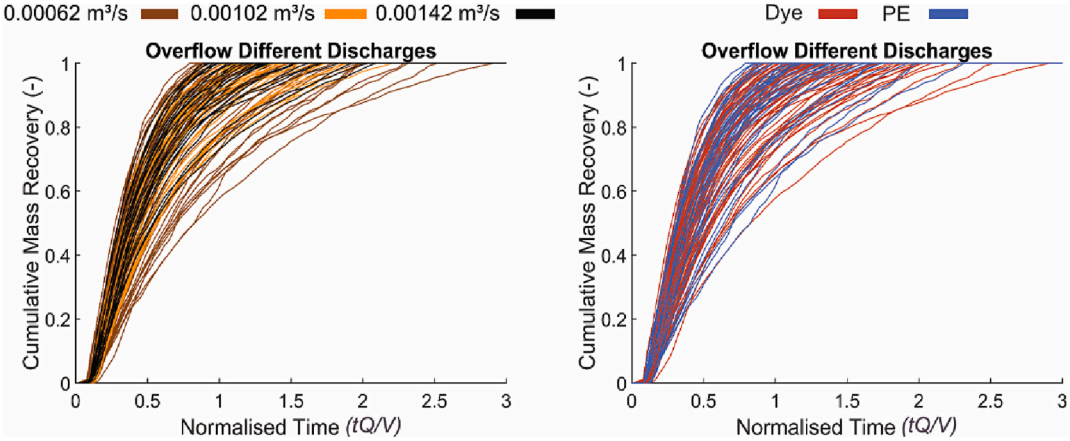

Fig. 4. Dye and PE CRTDs across all discharges for the PB and FB overflow scenarios.

took marginally longer to reach the outlet pipe and the top of the manhole with the largest difference occurring in the overflow scenarios (Table 3). To investigate the difference in MR between dye and PE for the manhole overflows CRTD profiles are plotted across all discharges in Fig. 4. When normalised through tQ/V dye and PE CRTD profiles were similar where dye demonstrated a slightly larger range at the end of its distribution with tQ/V reaching 2.8 compared to 2.25 for PE. However, this wasn't significant when t_m or t_{70} was compared (Welch's t-test $p > 0.05$). A clear pattern can be seen with Q due to a large range of 0.75–3 for 0.00062 m^3/s and the average steepness of the profile increasing with the other discharges.

3.3. ADZ and deconvolution

Results from the ADZ and DM analysis are presented in Table 1 and visualized in Fig. 5. The ADZ predicted dye downstream response curves better than PE for the variable and surcharge conditions and similarly for the overflow conditions. R_t^2 for the variable and 0.1 m surcharge ranged between 0.97 and 1.00 for dye and 0.79–0.89 for PE. This was greater for both concentrations than the higher surcharge conditions (0.25 and 0.4 m) which ranged from 0.66 to 0.7 for dye and 0–0.2 for PE when averaged (Table 1). Both dye and PE displayed corresponding R_t^2 between 0.9 and 0.95 for PB and FB overflows, respectively. Changing discharges between the circle and square manhole had no effect on the ADZ's predictive capability. The DM showed a high R_t^2 across all conditions for both dye and PE with a small range of 0.97–1.00. PE at a 0.25 m surcharge and a Q of 0.00102 m^3/s displayed the only mean R_t^2 value below 0.99. When averaged across all conditions R_t^2 was 0.89 for dye and 0.60 for PE using the ADZ and 1.00 for dye and 0.99 for PE using the DM. R_t^2 for the ADZ and DM displayed no significant difference between manhole geometries (Welch's t-test $p > 0.05$). The ADZ overpredicts the area under the curve for the RTDs receding limb when the difference between the start and end of the RTD was greater than approximately 10 s for the Q of 0.00102 m^3/s (Fig. 5). The ADZ also overpredicts the maximum value of the peak due to greater surcharges causing a lower R_t^2, with a greater difference for PE than dye. R_t^2 is greater for the overflow PB outlet condition due to the 5 % cut-off for the overflow conditions compared to 1 % for the others. As the y-axis is divided through by the peak concentration in Fig. 5, enabling dye and PE to be plotted on the same graph, the overprediction of the peak value cannot be seen in Fig. 5.

3.4. Flow visualization

To further validate the results and capture temporal snapshots of the tracer dynamics in the physical model, flow visualization techniques were adopted. Solute and PE interactions within the manhole were captured at a constant imaging rate of 60 frame per seconds once the tracer entered the manhole (Fig. 6). Pictures of dye movement for the first 5 s for all the conditions in the circular manhole are shown in Fig. 6a and PE movement in Fig. 6b for the 0.25 m and PB scenarios. Fig. 6a clearly shows the different degrees of mixing taking place across the different surcharges and reinforces the data analysis explained above (§ 3.1–3.3). The variable and 0.1 m surcharges were well-mixed almost instantly once the dye reaches the manhole whilst at higher surcharges the initial pulse expands as it passes through the manhole where a portion consequently hits the manhole side and rises upwards towards the surface conforming with submerged jet theory (Beg et al., 2017; Pedersen and Mark (1990); Sokáč and Velísková, 2021). Fig. 6b revealed PE followed the same pathways as dye in Fig. 6a and the faster velocities and subsequently higher concentrations moved up the side of the manhole above the outlet pipe. Analogous results were achieved for the square manhole. PE was not injected on mass into the manholes across all conditions due to the production costs of fluorescently tagged PE and potential impact of the PE ending up in the environment despite filtering precautions being taken.

4. Discussion

4.1. Hydraulic characteristics

The major loss in K after a higher $\frac{S}{P_d}$ of 2 for 0.00102 and 0.00142 m^3/s within the square and circle manholes reinforces previous data observed by Beg et al. (2017) & Jimoh (2015). The flow through a manhole experiences a loss of energy due to expansion and compression as it passes and exits through the manhole in the variable, 0.1, 0.25, and 0.4 m surcharges. While for the one- and two-exit overflow conditions, there was an increase in energy in the outflow pipe due to the rise in pressure from the partial and full closure of SG1 (resembling blockages in the pipe), resulting in negative head loss values. The full closure of SG1 in the FB condition creates enough pressure to nullify the effect Q has on K for both manholes (Fig. 2b). The circle manhole has greater head losses for the Q of 0.00142 m^3/s at an $\frac{S}{P_d}$ of 2 likely due to the relative increase in volume in the square manhole when compared to the circle manhole at higher surcharge depths causing the circular geometry to distribute turbulence more uniformly throughout. Furthermore, this difference was negligible when velocity was considered due to the square manhole containing a greater K. Both the observed head loss and head loss coefficient results correspond well to the mechanism where at low surcharge depths, the water surface has greater interaction with the incoming jet, resulting in greater flow exchange, high head losses, and greater mixing. This is because the incoming jet at lower surcharges

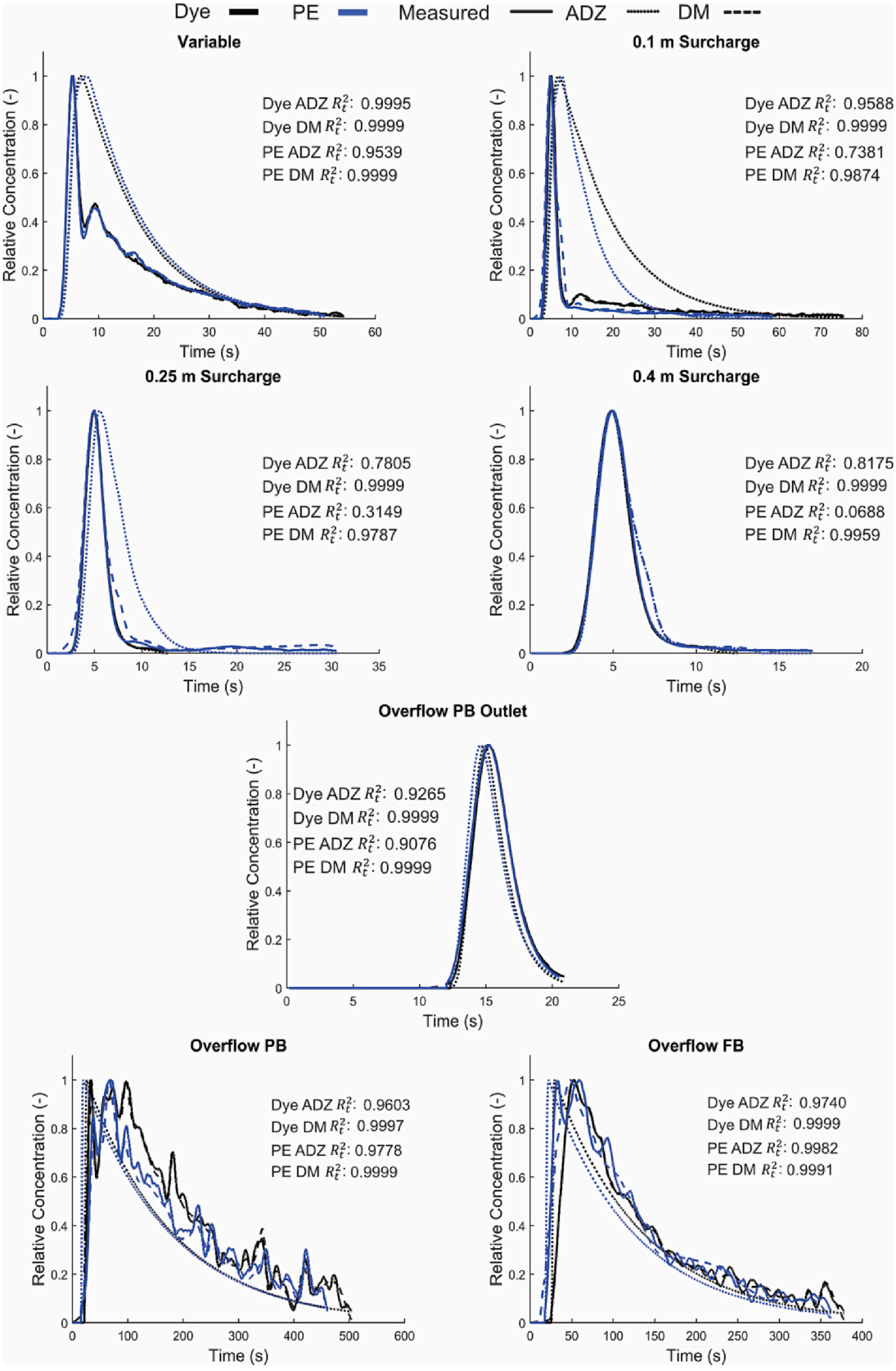

Fig. 5. Sample RTD goodness-of-fit within the square manhole for each condition at 0.00102 m^3/s using the ADZ and DM.

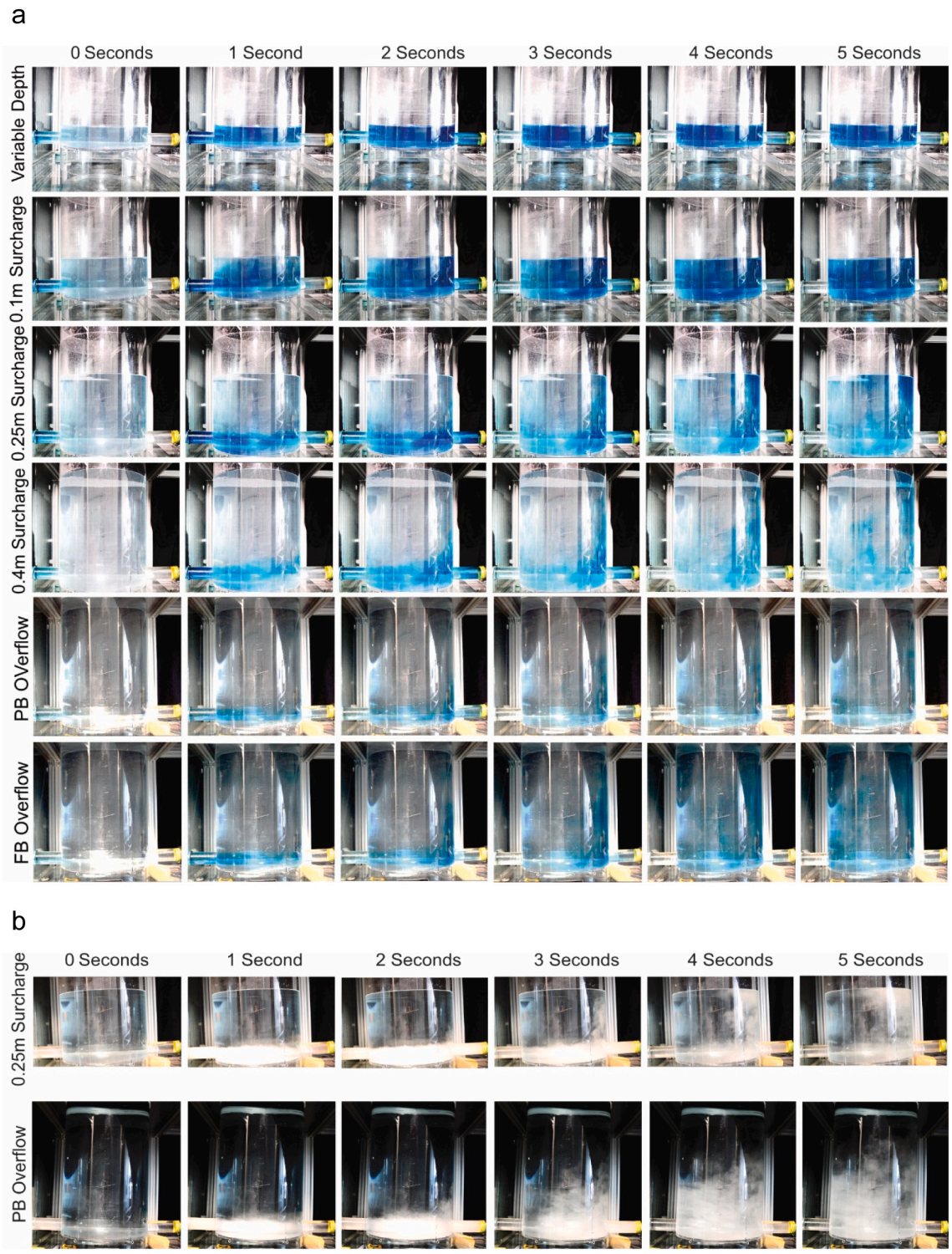

Fig. 6. a. Pictures of instantaneous solute injections for each experimental condition for the first 5 s at 0.00102 m^3/s.
b. Pictures of instantaneous PE injections for the 0.25 m and PB conditions for the first 5 s at 0.00102 m^3/s.

causes the water surface to oscillate which generates a lot of turbulence within the manhole (Mark and Ilesanmi-Jimoh, 2016). At high surcharge depths, the interaction between the water surface and incoming jet is reduced, resulting in a lower head loss and less mixing (Fig. 2a). At 0.00062 m^3/s K increased with $\frac{S}{P_d}$ between 0.08 and 2.00 due to the surcharge depth being just above that of the pipes for the variable condition ($\frac{S}{P_d} = 0.08$) resulting in very little head loss.

4.2. RTDs and CRTDs

Three distinct RTD and CRTD profiles indicate varying flow structures across the five different surcharges, including the PB scenario, when measured from the outlet conforming with Sonnenwald et al. (2021) example CRTDs for different mixing processes in manholes (Fig. 3a). The variable condition contained large amounts of mixing within a one-cell system inside the manhole, whilst the 0.25 and 0.4 m

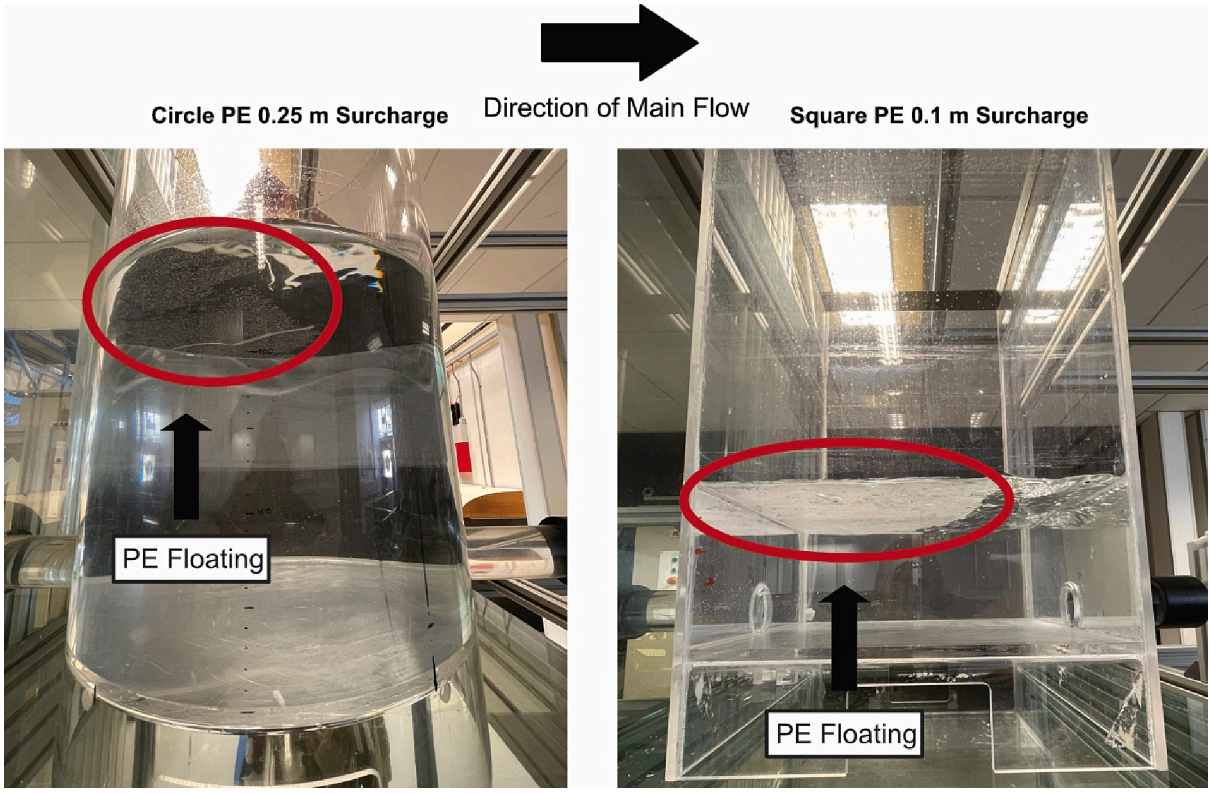

Fig. 7. Pictures displaying PE floating at the surface above the manhole inlet pipe for both the circle (left) and square (right) manholes at 0.25 m and 0.1 m surcharges respectively.

surcharges along with the PB condition correspond to a two-cell system with one containing a preferential flow path at the base of the manhole and the other a dead zone where little mixing occurs. The 0.1 m surcharge represents a transitional phase between the two and was unique due to being around the $\frac{S}{P_d}$ ratio of 2–2.5 stated by Guymer et al. (2005) and Lau et al. (2008). This is embodied by a steep rising CRTD profile demonstrating plug flow followed by a shallow profile for the remaining 40 % cumulative mass that enters the outlet pipe after mixing within the manhole and resulting in the largest t_m for any of the variable and surcharge conditions. The last 5–15 % cumulative mass for 0.25 and 0.4 m surcharges indicate that a small portion of both dye and PE reaches the outlet pipe after missing the outlet in the initial pulse and consequently mixing within the manhole itself.

The PB and FB conditions both demonstrate shallower profiles when exiting through the top of the manhole but the pressure created by the blocked outlet pipe produced a smaller t_m and faster velocities within the FB scenario. Low S_c values across all conditions signify large amounts of short-circuiting taking place, which is desirable in manholes. Short-circuiting transpired the most for the higher surcharges of 0.25 m, 0.4 m and PB outlet scenario but still occurred for the variable and 0.1 m surcharge conditions with a higher percentage of the concentration mass experiencing mixing within the manholes. S_c values between 0.31 and 0.38 for the FB condition indicate that preferential flow paths above the outlet were still occurring within the manhole even though the outlet pipe was fully blocked.

Although *HE* was the lowest at higher surcharges, the corresponding pollutants that were retained remain within a dead zone at the top of the manhole and do not exit via the outlet pipe (Fig. 7). This was confirmed through a low MR in the outlet pipe for the 0.25 and 0.4 m surcharges and a high MR for the PB overflow scenario at the top of the circle and square manholes. Low 0.25 and 0.4 m surcharge MR indicates a higher portion of dye and PE mass was remaining in the system near the top of the manhole subsequently reducing outlet pipe MR while potentially increasing manhole overflow recovery for the PB scenario (Table 3). Although having a higher outlet pipe MR (Table 3), PE retention within the dead zone still occurred for the 0.1 m surcharge as shown in the square manhole in Fig. 7 despite the water surface showing signs of undulation. This indicates the undulation was not yet significant enough to reintroduce PE below the surface, suggesting that PE requires significantly higher discharges and/or a $\frac{S}{P_d} < 2$ to leave the dead zone after floating on the water surface in manholes.

The change from 20 to 10 Hz on the fluorometers enabled logging times to increase without LABVIEW timing out for the overflow tests but also inflated MR for the PB overflow scenario. At 10 Hz the entire concentration mass for the fast inlet pipe velocities of 0.46 ± 0.0056, 0.65 ± 0.012, and 0.85 ± 0.00581 m/s (0.00062, 0.00102, and 0.00142 m^3/s discharges) was not captured thus reducing the total area of the inlet pipe concentration curves when compared against the captured concentration mass travelling at slow velocities at the top of the manhole (Fig. 3a & Fig. S2a). This had less of an effect on the slowest inlet pipe Q of 0.00062 m^3/s but as a precaution all MRs within the PB condition have been labelled with an asterisk (*) in Table 3. These MRs should then not be taken at their absolute value but can be compared directly against one another (dye vs PE). For future tests, running a minimum of 20 Hz is recommended to adequately capture MR within manhole flows. It is expected the true MR for the PB scenario in the outlet pipe would be analogous to the 0.25 and 0.4 m surcharges with approximately 47–67 % exiting through the outlet pipe without mixing and the remaining 33–53 % exiting the outlet pipe after circulating within the manhole, getting stuck in the dead zone, or exiting via the top of the manhole when overflowing. This was in accordance with the particle image velocimetry data from Beg et al. (2017) displaying high standard deviation near inlet, outlet, and jet expansion zones for solutes.

Dominant vertical velocities and preferential flow paths up the outlet side of the manholes cause a portion of the PE injection mass to reach the surface where it gets pushed to the inlet side of the manhole and it

remains for both geometries (Figs. 6b & 7). As a result, concentrations were stored within the dead zone and water surface at the top of the overflowing manhole above the inlet pipe and only exit after a significant amount of time has passed or a large pipe blockage or flooding event occurs with the bulk of the initial concentration mass previously having already moved through in both circle and square manhole configurations. Combined with PE exhibiting lower MR across all conditions and the largest percent difference between dye and PE happening within the overflow tests, it is reasonable to assume that PE may disperse differently to solutes within dead zones or when subjected to flows that contain higher vertical velocities towards the water surface than velocities in the longitudinal direction because of it being a solid particle with a slightly less than neutral buoyancy (0.91–0.97 g/cm^3). In dead zones, the force of advection may not be significant enough to influence PE movement resulting in PE floating to the surface and being subjected to surface tension where it struggles to be resuspended below the surface, which cannot happen to solutes. This phenomenon happens to approximately 17.3 ± 7.9 % of the injected PE mass when averaged. Due to the high nutrient loads in sewage water, elevated water temperatures during summer months, and stagnant water within surcharging manholes, there is a potentially serious concern regarding the risk of pathogenic and chemical contamination to wildlife and humans due to pathogens such as *E. coli* being able to form cohesive groups in biofilms on microplastic surfaces (Hou et al., 2021; Song et al., 2020). These exposed microplastics can then become vectors for pathogens that contain greater antibiotic resistance and virulence due to the favourable environmental conditions at the top of surcharging manholes (Hou et al., 2021; Song et al., 2020).

If isolated at specific real-world manhole configurations, microplastics possessing a neutral buoyancy or lower (such as PE and polypropylene) may be filtered at these manhole "hotspots", providing the correct technology is in place, thus preventing them from contaminating the environment. Nevertheless, RTD indices showed the bulk of the injected PE mass followed the same pathways as Rhodamine WT dye within manhole flows conforming with Abolfathi et al. (2020), Cook et al. (2020), and Stride et al.'s (2023) findings. More research is needed to determine the underlying transport processes of microplastics within dead zones and how they impact microplastic fate in each flow domain. The addition of a manhole cover expected in streets was not included in this study and thus the results omit the effects of different manhole covers on pollution transport in overflowing conditions. Furthermore, the occurrence of sediment and deposits in circular sewer pipes have been shown to decrease mixing, almost linearly decreasing flow rates (Sokáč and Velísková, 2021) and should be considered in real-world settings.

4.3. Modelling effectiveness

The ADZ was shown to be reasonably effective for the variable, 0.1 m surcharge, and overflow conditions exiting via the top of the manhole for both PE and dye based purely on R_t^2. But as Fig. 5 shows the receding limb was often overpredicted as the ADZ does not account for the increased retention time after the initial pulse and mixing within the manhole creating a steeper receding gradient. The ADZ was consistently better at predicting the mixing of dye than PE across all conditions, especially at 0.25 and 0.4 m surcharges where the model struggled and showed almost no predictive capability for PE. As a result, in agreement with Guymer et al. (2005) the ADZ is not suitable to predict mixing for solutes or microplastics in the outlet pipe of circle or square surcharged manholes. In contrast, the predictive capability of the DM was excellent across all conditions for both dye and PE making it the first model to adequately predict microplastic mixing within a complex flow regime. This proves that deconvolution can be successfully implemented for solid particles of a near neutral buoyancy in both circle and square manholes at a variety of discharges and surcharges.

Other factors such as size, type, and shape need to be researched further to identify where the model fails to predict the mixing of microplastics in manholes and assess its upper and lower limits. Overall, the results from this study were in line with several mixing studies for predicting solute mixing in manholes of different shapes, sizes, and surcharges (Guymer and Stovin (2011); Jimoh and Abolfathi, 2022; Sonnenwald et al., 2014; Sonnenwald et al., 2015) and widens their applicability to solid particles of a near neutral buoyancy such as PE. Results also improve on existing studies by demonstrating that solid particles disperse differently to solutes in dead zones present within manholes.

5. Conclusions

The transport characteristics of pollutants (i.e. solute and microplastics) have been quantified through fluorometric tracer studies in a circle and square manhole configurations under different flow and blockage conditions. The two blockage conditions resulted in the manhole overflowing, which was used to represent real-world flooding scenarios. Two manhole shapes, three inlet pipe discharges, and six surcharge configurations (seven if you include the overflow PB outlet scenario) were tested under full pipe flow. Head losses were experienced across all variable and surcharge conditions with greater losses at higher discharges with no significant differences between manhole geometries. Head loss was negative for the overflow conditions where the pressure in the outlet pipe increased the flow energy. The transport of neutrally buoyant microplastics represented by PE was quantified, where the bulk mass followed the same transport pathways as solutes except for 17.3 ± 7.9 % that was retained at the surface or in the dead zone above the manhole inlet. Consequently, a portion of neutrally buoyant microplastics will only exit after a large amount of time has passed causing them to be at risk of pathogenic or chemical contamination, after being immobilized in stagnant sewage water, and will only be released after a large pipe blockage or flooding event occurs (causing them to be released into urban areas) or the manhole surcharge decreases and the water surface undulates significantly causing them to exit through the outlet pipe. At the time of publishing, this is the first recorded instance where microplastics of a near neutral buoyancy disperse differently to solutes within the water column of a non-saline system.

The ADZ's predictive capability was inferior across all conditions tested for PE when compared to the representative solute. This inferiority for PE modelling was especially significant in the outlet pipe above the surcharge depth ratio of 2 where the model had little to no accuracy. The DM demonstrated an excellent predictive capability for both solutes and PE making it the most robust model proven to be capable of accurately predicting microplastic mixing in manholes and urban drainage systems. No differences were found in determining and modelling the mixing of solutes and PE between circle and square manholes. This study does not represent the full scope of microplastic physical properties that would be encountered in a manhole system. Future research should seek to quantify the transport of microplastics with different physical properties, including size, shape, and density along with different manhole angles, sizes, plunging, and benching. Nevertheless, this study forms the foundation for further research on microplastic movement in sewer systems.

Declarations

We confirm that none of the material has been published or is under consideration for publication elsewhere, and we have no conflicts of interest to declare. All data used in the analysis is available at the online repository of the University of Warwick, WRAP: https://wrap.warwick.ac.uk/177507.

CRediT authorship contribution statement

Ben Stride: Conceptualization, Data curation, Formal analysis, Funding acquisition, Investigation, Methodology, Project administration, Resources, Software, Validation, Visualization, Writing – original draft, Writing – review & editing. **Charlotte Dykes:** Conceptualization, Data curation, Investigation, Methodology, Visualization, Writing – review & editing. **Soroush Abolfathi:** Formal analysis, Investigation, Project administration, Software, Supervision, Validation, Visualization, Writing – review & editing. **Modupe Jimoh:** Formal analysis, Resources, Software. **Gary D. Bending:** Supervision, Writing – review & editing. **Jonathan Pearson:** Conceptualization, Formal analysis, Investigation, Methodology, Project administration, Resources, Supervision, Validation, Writing – review & editing.

Declaration of competing interest

The authors declare that they have no known competing financial interests or personal relationships that could have appeared to influence the work reported in this paper.

Data availability

Physical modelling data is available at the online repository of the University of Warwick, WRAP: https://wrap.warwick.ac.uk/177507.

Acknowledgments

Funding was provided by the Natural Environmental Research Council (NERC) and The Central England NERC Training Alliance (CENTA). We also acknowledge our Civil Engineering Technicians Ian Bayliss, Huw Edwards, Joel Whittle, and Iain Brown for help in setting up the experiment.

NERC grant NE/S007350/1 (243303, BS)

Appendix A. Supplementary data

Supplementary data to this article can be found online at https://doi.org/10.1016/j.scitotenv.2023.165683.

References

Abolfathi, S., Cook, S., Yeganeh-Bakhtiary, A., Borzooei, S., Pearson, J., 2020. Microplastics transport and mixing mechanisms in the nearshore region. Coast. Eng. Proc. 36, 63. https://doi.org/10.9753/icce.v36v.papers.63.

Beer, T., Young, P.C., 1983. Longitudinal dispersion in natural streams. J. Environ. Eng. 109 (5), 641–650. https://doi.org/10.1061/(asce)0733-9372(1983)109:5(1049).

Beg, M.N.A., Carvalho, R.F., Tait, S., Brevis, W., Rubinato, M., Schellart, A., Leandro, J., 2017. A comparative study of manhole hydraulics using stereoscopic PIV and different RANS models. Water Sci. Technol. 2017 (1), 87–98. https://doi.org/10.2166/wst.2018.089.

Beg, M.N.A., Carvalho, R.F., Leandro, J., 2019. Effect of manhole molds and inlet alignment on the hydraulics of circular manhole at changing surcharge. Urban Water J. 16 (1), 33–44. https://doi.org/10.1080/1573062X.2019.1611887.

Beg, M.N.A., Rubinato, M., Carvalho, R.F., Shucksmith, J.D., 2020. CFD modelling of the transport of soluble pollutants from sewer networks to surface flows during urban flood events. Water 12 (9), 2514. https://doi.org/10.3390/w12092514.

Cook, S., Chan, H.L., Abolfathi, S., Bending, G.D., Schäfer, H., Pearson, J.M., 2020. Longitudinal dispersion of microplastics in aquatic flows using fluorometric techniques. Water Res. 170 (3), 115337 https://doi.org/10.1016/j.watres.2019.115337.

Danckwerts, P.V., 1953. Continuous flow systems. Chem. Eng. Sci. 2 (1), 1–13. https://doi.org/10.1016/0009-2509(53)80001-1.

de Man, H., van den Berg, H.H.J.L., Leenen, E.J.T.M., Schijven, J.F., Schets, F.M., van der Vliet, J.C., van Knapen, F., de Roda Husman, A.M., 2014. Quantitative assessment of infection risk from exposure to waterborne pathogens in urban floodwater. Water Res. 48 (1), 90–99. https://doi.org/10.1016/j.watres.2013.09.022.

Frias, J.P.G.L., Nash, R., 2019. Microplastics: finding a consensus on the definition. Mar. Pollut. Bull. 138 (9), 145–147. https://doi.org/10.1016/j.marpolbul.2018.11.022.

GebreEgziabher, M., Demissie, Y., 2020. Modeling urban flood inundation and recession impacted by manholes. Water 12 (4), 15–20. https://doi.org/10.3390/W12041160.

Guymer, I., O'Brien, R., 2000. Longitudinal dispersion due to surcharged manhole. J. Hydraul. Eng. 126 (2), 137–149. https://doi.org/10.1061/(asce)0733-9429(2000)126:2(137).

Guymer, I., Stovin, V.R., 2011. One-dimensional mixing model for surcharged manholes. J. Hydraul. Eng. 137 (10), 1160–1172. https://doi.org/10.1061/(asce)hy.1943-7900.0000422.

Goodarzi, D., Mohammadian, A., Pearson, J., Abolfathi, S., 2022. Numerical modelling of hydraulic efficiency and pollution transport in waste stabilization ponds. Ecol. Eng. 182 (9), 106702 https://doi.org/10.1016/j.ecoleng.2022.106702.

Guymer, I., Dennis, P., Saiyudthong, C., 2005. Diameter and surcharge effects on solute transport across surcharged manholes. J. Hydraul. Eng. 131 (4), 312–321. https://doi.org/10.1061/(asce)0733-9429(2005)131:4(312).

Hou, D., Hong, M., Wang, Y., Dong, P., Cheng, H., Yan, H., Yao, Z., Li, D., Wang, K., Zhang, D., 2021. Assessing the risks of potential bacterial pathogens attaching to different microplastics during the summer–autumn period in a mariculture cage. Microorganisms 9 (9), 1909. https://doi.org/10.3390/microorganisms9091909.

Jenner, L.C., Rotchell, J.M., Bennett, R.T., Cowen, M., 2022. Detection of microplastics in human lung tissue using μ FTIR spectroscopy. Sci. Total Environ. 831 (7), 154907 https://doi.org/10.1016/j.scitotenv.2022.154907.

Jimoh, M., 2015. Solute mixing due to square manholes. Ph.D thesis Dept. of Civil Engineering,. University of Warwick.

Jimoh, M., Abolfathi, S., 2022. Modelling pollution transport dynamics and mixing in square manhole overflows. J. Water Process Eng. 45 (2), 102491 https://doi.org/10.1016/j.jwpe.2021.102491.

Jones, J.I., Vdovchenko, A., Cooling, D., Murphy, J.F., Arnold, A., Pretty, J.L., Spencer, K.L., Markus, A.A., Vethaak, A.D., Resmini, M., 2020. Systematic analysis of the relative abundance of polymers occurring as microplastics in freshwaters and estuaries. Int. J. Environ. Res. Public Health 17 (24), 1–12. https://doi.org/10.3390/ijerph17249304.

Kerenyi, K., Jones, J.S., Stein, S., 2007. Junction Loss Experiments: Laboratory Report. 66.

Lau, S., Stovin, V., Guymer, I., 2008. Scaling the solute transport characteristics of a surcharged manhole. Urban Water J. 5 (1), 33–42. https://doi.org/10.1080/15730620701737249.

Mark, O., Ilesanmi-Jimoh, M., 2016. An analytical model for solute mixing in surcharged manholes. Urban Water J. 14 (5), 443–451. https://doi.org/10.1080/1573062X.2016.1179335.

Österlund, H., Blecken, G., Lange, K., Marsalek, J., Gopinath, K., Viklander, M., 2023. Microplastics in urban catchments: review of sources, pathways, and entry into stormwater. Sci. Total Environ. 858 (10), 159781 https://doi.org/10.1016/j.scitotenv.2022.159781.

Pedersen, F.B., Mark, O., 1990. Head losses in storm sewer manholes: submerged jet theory. J. Hydraul. Eng. 116 (11), 1317–1328. https://doi.org/10.1061/(asce)0733-9429(1990)116:11(1317).

Persson, J., 2000. The hydraulic performance of ponds of various layouts. Urban Water J. 2 (3), 243–350.

Plastics Europe, 2021. Plastics the facts 2021, 1–34. Retrieved 19th August 2022 from. https://plasticseurope.org/knowledge-hub/plastics-the-facts-2021/.

Rutherford, J.C., 1994. River Mixing. John Wiley and Sons, New York.

Sana, S.S., Dogiparthi, L.K., Gangadhar, L., Chakravorty, A., Abhishek, N., 2020. Effects of microplastics and nanoplastics on marine environment and human health. Environ. Sci. Pollut. Res. 27 (36), 44743–44756. https://doi.org/10.1007/s11356-020-10573-x.

Schreiber, C., Heinkel, S.-B., Zacharias, N., Mertens, F.-M., Christoffels, E., Gayer, U., Koch, C., Kistemann, T., 2019. Infectious rain? Evaluation of human pathogen concentrations in stormwater in separate sewer systems. Water Sci. Technol. 80 (6), 1022–1030. https://doi.org/10.2166/wst.2019.340.

Sokáč, M., Velísková, Y., 2021. Impact of sediment layer on longitudinal dispersion in sewer systems. Water 13 (22), 3168. https://doi.org/10.3390/w13223168.

Song, J., Jongmans-Hochschulz, E., Mauder, N., Imirzalioglu, C., Wichels, A., Gerdts, G., 2020. The travelling particles: investigating microplastics as possible transport vectors for multidrug resistant E. coli in the Weser estuary (Germany). Sci. Total Environ. 720 (2), 137603 https://doi.org/10.1016/j.scitotenv.2020.137603.

Sonnenwald, F., Stovin, V., Guymer, I., 2014. Configuring maximum entropy deconvolution for the identification of residence time distributions in solute transport applications. J. Hydrol. Eng. 19 (7), 1413–1421. https://doi.org/10.1061/(asce)he.1943-5584.0000929.

Sonnenwald, F., Stovin, V., Guymer, I., 2015. Deconvolving smooth residence time distributions from raw solute transport data. J. Hydrol. Eng. 20 (11), 04015022. https://doi.org/10.1061/(asce)he.1943-5584.0001190.

Sonnenwald, F., Mark, O., Stovin, V., Guymer, I., 2021. Predicting manhole mixing using a compartmental model. J. Hydraul. Eng. 147 (12), 1–12. https://doi.org/10.1061/(asce)hy.1943-7900.0001951.

Stovin, V.R., Grimm, J.P., Lau, S.-T.D., 2008. Solute transport modeling for urban drainage structures. J. Environ. Eng. 134 (8), 640–650. https://doi.org/10.1061/(asce)0733-9372(2008)134:8(640).

Stovin, V., Guymer, I., Lau, S.-T.D., 2010. Dimensionless method to characterize the mixing effects of surcharged manholes. J. Hydraul. Eng. 136 (5), 318–327. https://doi.org/10.1061/(asce)hy.1943-7900.0000183.

Stride, B., Abolfathi, S., Odara, M.G.N., Bending, G.D., Pearson, J., 2023. Modelling microplastic and solute transport in vegetated flows. Water Resour. Res. 59 (5), e2023WR034653 https://doi.org/10.1029/2023WR034653.

Ta, C.T., Brignal, W.J., 1998. Application of computational fluid dynamics technique to storage reservoir studies. Water Sci. Technol. 37 (2), 219–226.

Taylor, G., 1954. The dispersion of matter in turbulent flow through a pipe. Proc. R. Soc. Lond. A Math. Phys. Sci. 223 (1155), 446–468. https://doi.org/10.1098/rspa.1954.0130.

Wallis, S.G., Beven, K.J., 1989. Transport in stream channels. Proc. Inst. Civ. Eng. 87 (1), 1–22.

Zhang, E., Kim, M., Rueda, L., Rochman, C., VanWormer, E., Moore, J., Shapiro, K., 2022. Association of zoonotic protozoan parasites with microplastics in seawater and implications for human and wildlife health. Sci. Rep. 12 (1), 1–11. https://doi.org/10.1038/s41598-022-10485-5.

Ziccardi, L.M., Edgington, A., Hentz, K., Kulacki, K.J., Kane Driscoll, S., 2016. Microplastics as vectors for bioaccumulation of hydrophobic organic chemicals in the marine environment: a state-of-the-science review. Environ. Toxicol. Chem. 35 (7), 1667–1676. https://doi.org/10.1002/etc.3461.